Confinement in Carbon Nanospace-Induced Production of KI Nanocrystals of High-Pressure Phase

Koki Urita,[†] Yuichi Shiga,[‡] Toshihiko Fujimori,[§] Taku Iiyama,[||] Yoshiyuki Hattori,[⊥] Hirofumi Kanoh,[‡] Tomonori Ohba,[‡] Hideki Tanaka,[#] Masako Yudasaka,[∇] Sumio Iijima,[∇] Isamu Moriguchi,[†] Fujio Okino,[⊥] Morinobu Endo,[§] and Katsumi Kaneko*,[‡,§]

[†]Department of Engineering, Nagasaki University, 1-14 Bunkyo-machi, Nagasaki 852-8521, Japan

[‡]Graduate School of Science, Chiba University, 1-33 Inage-ku, Yayoi-cho, Chiba 263-8522, Japan

[§]Research Center for Exotic Nanocarbons (JST), Shinshu University, 4-17-1 Wakasato, Nagano 380-8553 Japan

[||]Department of Chemistry, Faculty of Science, Shinshu University, 3-1-1, Asahi, Matsumoto, Nagano 390-8621, Japan

[⊥]Faculty of Textile Science and Technology, Shinshu University, 3-15-1 Tuneda, Ueda 386-8567, Japan

[#]Department of Chemical Engineering, Kyoto University, Nishikyo-ku, Kyoto 615-8510, Japan

[∇]National Institute of Advanced Industrial Science and Technology (AIST), Tsukuba 205-8565, Japan

S *Supporting Information*

ABSTRACT: An outstanding compression function for materials preparation exhibited by nanospaces of single-walled carbon nanohorns (SWCNHs) was studied using the B1-to-B2 solid phase transition of KI crystals at 1.9 GPa. High-resolution transmission electron microscopy and synchrotron X-ray diffraction examinations provided evidence that KI nanocrystals doped in the nanotube spaces of SWCNHs at pressures below 0.1 MPa had the super-high-pressure B2 phase structure, which is induced at pressures above 1.9 GPa in bulk KI crystals. This finding of the super-compression function of the carbon nanotubular spaces can lead to the development of a new compression-free route to precious materials whose syntheses require the application of high pressure.

Confinement of materials in nanometer-scale spaces induces unique phenomena different from those of the bulk phases.[1] When organic liquids and water are confined in few-nanometer spaces, they have solidlike structures. The viscosity of water, however, remains comparable to its bulk value.[2] The remarkable contrast of the fluidity of water with the behavior of nonassociative organic liquids is to reduce the formation of hydrogen-bonded networks of water.[2,3] Since a biological membrane constructed from hydrophobic elements has nanospaces for separations of the inside and outside of cells and control of the movement of substances, the fluidity of water in confined carbon nanospaces relates closely to a biological system. Carbon nanospaces also play an important role as reaction fields for molecules and ions, as they are significantly different from surfaces because the interaction potential of a molecule with the nanospace walls is remarkably enhanced. The confinement of molecules in carbon nanospaces can induce high-pressure gas-phase reactions at ambient pressure. We clearly showed that the gas-phase disproportionation reaction of $(NO)_2$ to N_2O and NO_2 above 20 MPa occurs efficiently in slit-shaped carbon nanospaces.[4] We named the effect of carbon nanospaces a quasi-high-pressure effect. The quasi-high-pressure

effect of the slit-shaped nanopore spaces was also evidenced in the electrochemical reduction of CO_2 to CO by Saeki et al.[5] The confinement of molecular assemblies in carbon nanospaces also causes remarkable shifts in the freezing temperature.[6] Thus, confinement of materials in carbon nanospaces has promising potential applications in gas storage,[7] energy-storage devices,[8] and nanosized reaction cells.[9] We can expect that a cylindrical carbon nanospace should provide a more prominent confinement effect. Molecular simulations by Koga et al.[10] suggested that water encapsulated in a single-walled carbon nanotube (SWCNT) forms a new one-dimensional ice phase not seen in bulk ice and shows a new solid–liquid critical point. High-resolution transmission electron microscopy (HRTEM) studies by Sloan and co-workers[11] indicated the marked confinement effect of SWCNTs. They showed that the spatial confinement of KI crystals led to a reduction in the coordination of the ambient-pressure B1 phase ($Fm\overline{3}m$). Therefore, a powerful combined study of the confinement of materials in carbon tubular nanospaces using HRTEM and synchrotron X-ray diffraction (XRD) should open new fields of chemistry and physics. In this study, we focused on the structural phase transition of KI crystals from B1 (space group $Fm\overline{3}m$, NaCl-type) to B2 (space group $Pm\overline{3}m$, CsCl-type) at 1.9 GPa[12] to clarify the intensive confinement effect of graphene-walled tubular nanospaces on nanocrystals.

Single-walled carbon nanohorns (SWCNHs) having graphene-walled tubular nanospaces were used here as the growth field of KI nanocrystals. SWCNHs have an assembly structure consisting of a large number of short-form SWCNTs possessing a horn-shaped cap with a diameter of 2−5 nm at one end.[13] A spherical assembly of SWCNHs with a uniform size of 80 nm has interparticle nanopores whose sizes range from 1 nm to several nanometers. According to the preceding study using N_2 adsorption measurements at 77 K,[14] the internal tubular space volume and interparticle nanopore volume (pore diameter <2 nm) are 0.50 and 0.11 mL g^{-1}, respectively. Furthermore, 30% of the

SWCNH particles are open, on the basis of the particle density of 1.25 g mL^{-1}; the available volume of internal tubular space is nearly twice the available interparticle nanopore volume. Hence, there are two sites in the SWCNH assembly for KI crystal growth (see Figure S1 in the Supporting Information): the external surfaces, which includes the narrow interparticle spaces, and the one-dimensional internal tubular spaces. Especially, the internal nanospaces constructed by the graphene walls of the SWCNHs can provide stable growth sites for KI nanocrystals. The SWCNHs were heated at 423 K in vacuo for 2 h prior to the KI doping treatment. Highly pure KI (Wako, 99.7%) was doped into the SWCNHs by heating mixtures of SWCNHs and KI at 1073 K for 8 h in a closed quartz cell. The amount of mixed KI was sufficient to fill the pore volume of the SWCNHs. The SWCNHs, KI, and KI-doped SWCNHs (KI@SWCNH) were sealed in a 0.5 mm Lindemann glass capillaries (Hilgenberg GmbH) for the synchrotron XRD measurements. These measurements were performed using beamline BL02B2 at SPring-8, where the wavelength of the incident X-rays was 0.1002(9) nm. KI@SWCNH sonicated in ethanol was dropped on a carbon grid for HRTEM observations. The atomic structures of KI in KI@SWCNH were directly observed using a high-resolution transmission electron microscopy (JEOL: JEM-2010) at an accelerating voltage of 200 kV. The HRTEM images were detected using a CCD camera (Gatan ORIUS SC1000).

HRTEM observation gives information only on KI nanocrystals that are stable in vacuo under electron irradiation. In fact, we could not observe clear images of KI@SWCNH after electron irradiation for a few minutes. We assumed that the stable image of KI nanocrystals did not stem from KI crystals on the external surface of the SWCNH assembly but from those in the confined internal tubular spaces. Since there were not enough holes in the carbon walls for migration of the KI nanocrystals, the nanocrystals should be stably kept in the internal tubular spaces during the sonication in ethanol and electron irradiation, in contrast to those on the external surfaces. The direct evidence for growth in the internal tubular space is shown in the cross-sectional HRTEM image in Figure S2. We observed only two types of stable HRTEM images for KI nanocrystals in the internal tube spaces. Figure 1 shows one type of HRTEM image of the KI nanocrystals. Here, it is important to consider that the predominant contrast derives from iodine atoms in the observed HRTEM images because potassium is a light element. The average atomic distances between the I atoms along the nanohorn axis (red square in Figure 1b) and perpendicular to the nanohorn axis (blue square in Figure 1b) were determined from the distances between the concavities of the contrast curves, as shown in Figure 1e,f, respectively. The observed image represents the ac plane of the KI crystal; the direction along the nanohorn axis corresponds to the c direction of the crystal, whereas the direction perpendicular to the nanohorn axis corresponds to the a or b direction of the crystal. The TEM image leads to lattice constants of $a = b = 0.35$ nm and $c = 0.38$ nm, which coincide with those of the anisotropic B2-type structure ($Pmmm$). In the case of the bulk phase, the B2-type structure must be prepared by compression with a high pressure of more than 1.9 GPa. Detailed information further comes from image simulation. Figure 1c shows a structural model of KI@SWCNH in the [010] direction. We used the SWCNT as a model to simulate the tube portion of the SWCNH, where yellow and green circles denote I and K atoms, respectively. Here, the platelike KI crystal ($Pmmm$) with lattice constants of $a = b = 0.35$ nm and $c = 0.38$ nm is aligned in the internal tubular space of a (13,13) SWCNT with
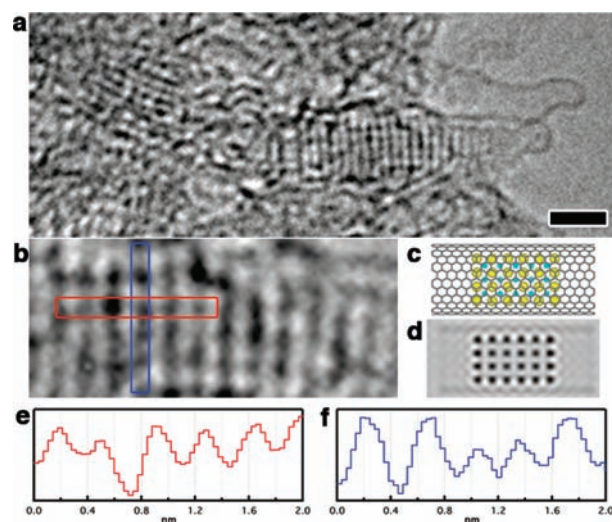

Figure 1. TEM image of the B2-type KI structure in an SWCNH. (a, b) TEM images of KI@SWCNH. The scale bar represents 2 nm. Contrast curve regions in the magnified TEM image (b) are specified by the red square along the nanohorn axis and the blue square perpendicular to the nanohorn axis. (c) Model of KI@SWCNH. The crystal system of KI in the SWCNH is $Pmmm$, and the SWCNH was constructed using a (13,13) armchair SWCNT with a diameter of ~1.7 nm. (d) Calculated image of the KI@SWCNH model in (c). (e, f) Contrast curves of the regions marked by the red and blue rectangles in (b).

a diameter of ~1.7 nm. We then obtained an image simulated with the multislice method,[15] as shown in Figure 1d. The iodine-originated simulation image exhibits good agreement with the observed HRTEM image. Thus, the HRTEM explicitly shows that confinement of KI in the internal tubular spaces of SWCNHs induces the formation of KI nanocrystals in the high-pressure B2 phase without compression by a pressure of more than 1.9 GPa.

We observed a well-aligned KI nanocrystal of another structure in the internal tubular space (see Figure S3). Each average atomic distance as determined from the contrast curves was 0.35 nm in the directions both of parallel and perpendicular to the nanohorn axis. Although it is hardly possible to distinguish the B1 and B2 structures from the length between two dark contrasts, the length of 0.35 nm corresponds to precisely half the lattice constant of the B1-type structure ($Fm\bar{3}m$) obtained from XRD analysis (see below). Thus, the observed KI nanocrystal should have the B1 structure. The iodine-originated simulation image with the anisotropically grown B1-type crystal is similar to the observed HRTEM image, agreeing with the HRTEM results reported by Meyer and Sloan.[11]

Synchrotron X-ray analyses of KI in SWCNHs should support intensively the above conclusion obtained by the HRTEM analyses. The synchrotron XRD patterns should originate from KI crystals grown at the external surface and internal tubular sites; the predominant KI crystals should be present on the external surfaces in the XRD measurement. Figure 2 shows the synchrotron XRD patterns of SWCNH, KI@SWCNH, and bulk KI crystals at room temperature. The XRD profile of the SWCNH (Figure 2a) shows split sharp peaks at $2\theta \approx 17°$, which is the (002) diffraction peak of the residual graphite in the SWCNH assembly core. Another asymmetric diffraction peak at $2\theta \approx 27°$ is assigned to 10 reflections of the turbostratic structures of SWCNH and the residual graphite. The XRD pattern of the bulk KI crystals (the bottom pattern in Figure 2a), whose lattice parameters are $a = b = c = 0.7063$ nm
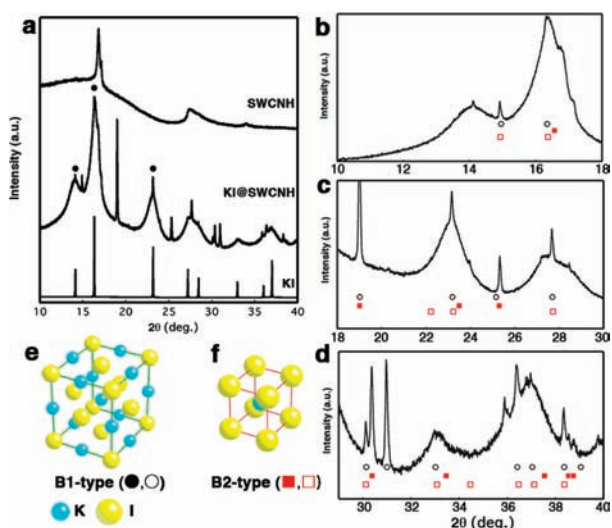
Figure 2. Synchrotron XRD patterns of SWCNH, KI@SWCNH, and KI. The wavelength was 0.01002(9) nm. (a) Overall XRD patterns from $2\theta = 10$ to $40°$. Peaks due to B1-type KI crystals are marked with ●. (b−d) Magnified XRD patterns of KI@SWCNH. Peaks due to an orthorhombic crystal-based structure (B1-type) with a slight anisotropy are marked with ○, and those for two types of slightly distorted B2-type structures are marked with ■ and □. (e, f) Crystal models of B1-type and B2-type structures of KI crystals, respectively.

and $\alpha = \beta = \gamma = 90°$, agrees well with the standard atmospheric-pressure B1-type KI phase ($Fm\overline{3}m$) in the literature.[16] Many sharp peaks of KI@SWCNH (marked with ● symbols) can be assigned to the B1-type KI crystal with a markedly anisotropic growth, because the intensity ratio is different from that of bulk KI crystals. As there are narrow one-dimensional interparticle spaces in the SWCNH assembly, the anisotropic growth should be accelerated as well as in the internal tube spaces.

However, there are clear peaks that cannot be assigned to KI in the B1-type phase ($Fm\overline{3}m$) or to the SWCNH. Figure 2b−d show magnified XRD patterns of KI@SWCNH in the 2θ ranges 10−18°, 18−30°, and 29−40°. The unassigned peaks must come from KI nanocrystals having structures different from the standard atmospheric-pressure B1-type crystal ($Fm\overline{3}m$). Since the synchrotron XRD can detect even the tiny amounts of KI crystals grown in internal tubular spaces, where the KI crystals are stably formed as shown in the HRTEM results, the KI crystals giving the unassigned peaks should be formed in the internal tube spaces. Some of the KI crystals should give rise to an anisotropic structure of the tetragonal crystal structure ($I4/mmm$) with lattice parameters of $a = 0.4993$ nm and $c = 0.6078$ nm, which is a slightly distorted structure of the ambient-pressure phase ($a = 0.7065$ nm, $Fm\overline{3}m$) that is close to the crystal structure observed by the HRTEM (Figure S3). These peaks are marked by ○ in Figure 2b−d, and the B1-type crystal structures are shown in Figure 2e.

However, the anisotropic structure of a tetragonal KI crystal alone could not completely account for the unassigned peaks. As the KI crystals formed in the internal tube spaces grow along the tube axis of SWCNHs, the peaks derived from the Miller planes parallel to tube axis should not show strong peaks. The residual XRD peaks can be assigned to two B2-type structures, the tetragonal ($P4/mmm$) structures having $a = 0.3485$ nm, $c = 0.3040$ nm and $a = 0.3530$ nm, $c = 0.3863$ nm, which are denoted by the red ■

and □ symbols, respectively. These two crystal structures are slightly distorted structures of the ideal B2-type high-pressure phase whose structural model is shown in Figure 2f. The intensive confinement of KI nanocrystals in the one-dimensional internal tubular spaces should induce the slight distortion. The synchrotron X-ray analyses can determine more exactly the crystal structure of the KI nanocrystals in the internal tubular spaces than the above HRTEM analyses. Although a few weak peaks could not be assigned, this result provides definite evidence for the presence of the KI nanocrystals in the high-pressure phase in spite of no application of high pressures of more than 1.9 GPa.

Both HRTEM and XRD analyses have explicitly shown that the confinement of KI nanocrystals in the cylindrical graphene-walled nanospaces of SWCNHs can induce the spontaneous growth of the high-pressure-phase structure, whose formation requires a pressure of more than 1.9 GPa in the case of the bulk solid. This high-pressure effect of the nanospaces of SWCNHs can be generally applicable to the synthesis of valuable high-pressure materials, which is promising for construction of sustainable chemistry and technology.

■ ASSOCIATED CONTENT

ⓢ Supporting Information. Model of crystal growth sites on SWCNHs and TEM images of a cross section of the tube part of KI@SWCNH and the B1-type KI structure in SWCNH. This material is available free of charge via the Internet at http://pubs.acs.org.

■ AUTHOR INFORMATION

Corresponding Author
kkaneko@shinshu-u.ac.jp

■ ACKNOWLEDGMENT

■ REFERENCES

(1) (a) Granick, S. *Science* **1991**, *253*, 1374–1379. (b) Iiyama, T.; Nishikawa, K.; Ohba, T.; Kaneko, K. *J. Phys. Chem.* **1995**, *99*, 10075–10076. (c) Gelb, L. D.; Gubbins, K. E.; Radhakrishnan, R.; Sliwinska-Bartkowiak, M. *Rep. Prog. Phys.* **1999**, *62*, 1573–1660. (d) Hashimoto, S.; Fujimori, T.; Tanaka, H.; Urita, K.; Ohba, T.; Kanoh, H.; Itoh, T; Asai, M.; Sakamoto, H.; Niimura, S.; Endo, M.; Rodriguez-Reinoso, F.; Kaneko, K. *J. Am. Chem. Soc.* **2011**, *133*, 2022–2024.

(2) Raviv, U.; Laurat, P.; Klein, J. *Nature* **2001**, *413*, 51–54.

(3) (a) Hummer, G.; Rasaiah, J. C.; Noworyta, J. P. *Nature* **2001**, *414*, 188–190. (b) Ohba, T.; Kanoh, H.; Kaneko, K. *Nano Lett.* **2005**, *5*, 227–230.

(4) Imai, J.; Souma, M.; Ozeki, S.; Suzuki, T.; Kaneko, K. *J. Phys. Chem.* **1991**, *95*, 9955–9960.

(5) Saeki, T.; Hashimoto, K.; Kimura, N.; Omata, K.; Fujishima, A. *J. Electroanal. Chem.* **1996**, *404*, 299–302.

10346

dx.doi.org/10.1021/ja202565r |*J. Am. Chem. Soc.* 2011, 133, 10344–10347

(6) (a) Miyahara, M.; Gubbins, K. E. *J. Chem. Phys.* **1997**, *106*, 2865–2880. (b) Kaneko, K.; Watanabe, A.; Iiyama, T.; Radhakrishan, R.; Gubbins, K. E. *J. Phys. Chem. B* **1999**, *103*, 7061–7063.

(7) Noguchi, D.; Tanaka, H.; Fujimori, T.; Kagita, H.; Hattori, Y.; Honda, H.; Urita, K.; Utsumi, S.; Wang, Z. M.; Ohba, T.; Kanoh, H.; Hata, K.; Kaneko, K. *J. Phys.: Condens. Matter* **2010**, *22*, No. 334207.

(8) Simon, P.; Gogotsi, Y. *Nat. Mater.* **2006**, *7*, 845–854.

(9) (a) Sun, L.; Banhart, F.; Krasheninnikov, A. V.; Rodríguez-Manzo, J. A.; Terrones, M.; Ajayan, P. M. *Science* **2006**, *312*, 1199–1202. (b) Rodríguez-Manzo, J. A.; Terrones, M.; Terrones, H.; Kroto, H. W.; Sun, L.; Banhart, F. *Nat. Nanotechnol.* **2007**, *2*, 307–311. (c) Koshino, M.; Niimi, Y.; Nakamura, E.; Kataura, H.; Okazaki, T.; Suenaga, K.; Iijima, S. *Nat. Chem.* **2010**, *2*, 117–124.

(10) Koga, K.; Gao, G. T.; Tanaka, H.; Zeng, X. C. *Nature* **2001**, *412*, 802–805.

(11) (a) Meyer, R. R.; Sloan, J.; Dunin-Borkowski, R. E.; Kirkland, A. I.; Novotny, M. C.; Bailey, S. R.; Hutchison, J. L.; Green, M. L. H. *Science* **2000**, *289*, 1324–1326. (b) Sloan, J.; Novotony, M. C.; Bailey, S. R.; Brown, G.; Xu, C.; Williams, V. C.; Friedrichs, S.; Flahaut, E.; Callender, R. L.; York, A. P. E; Coleman, K. S.; Green, M. L. H.; Dunin-Borkowski, R. E.; Hutchison, J. L. *Chem. Phys. Lett.* **2000**, *329*, 61–65.

(12) Asaumi, K.; Suzuki, T.; Mori, T. *Phys. Rev. B* **1983**, *28*, 3629–3533.

(13) Iijima, S.; Yudasaka, M.; Yamada, R.; Bandow, S.; Suenaga, K.; Kokai, F; Takahashi, K. *Chem. Phys. Lett.* **1999**, *309*, 165–170.

(14) Murata, K.; Miyawaki, J.; Yudasaka, M.; Iijima, S.; Kaneko, K. *Carbon* **2005**, *43*, 2817–2833. As an alternative model for an SWCNH, we assumed a closed SWCNT with a diameter of 3.3 nm and a length of 80 nm. The single wall density was 2.27 g mL^{-1}. Therefore, we could evaluate the particle density of closed SWCNTs using geometrical parameters. The evaluated particle density was 0.85 g mL^{-1}. Hence, the fraction of open SWCNHs was evaluated to be 0.3.

(15) Kirkland, E. J. *Advanced Computing in Electron Microscopy*; Springer: New York, 1998.

(16) Hambling, P. G. *Acta Crystallogr.* **1953**, *6*, 98.